Nanoscale

PAPER

View Article Online
View Journal | View Issue

Cite this: *Nanoscale*, 2016, **8**, 17608

Solution-processed nickel oxide nanoparticles with NiOOH for hole injection layers of high-efficiency organic light-emitting diodes†

Jeonggi Kim,[a] Hui Joon Park,[b,c] Costas P. Grigoropoulos,[d] Daeho Lee*[e] and Jin Jang*[a]

Received 8th June 2016,
Accepted 14th September 2016

DOI: 10.1039/c6nr04643f

www.rsc.org/nanoscale

Nickel oxide (NiO_x) nanoparticles (NPs) were synthesized by a solution-based method and NP films were used as hole injection layers (HILs) in organic light-emitting diodes (OLEDs). To evaluate the hole injection functionality of the NiO_x NP HIL, we compared the performance of OLEDs with three types of HILs: spin-coated PEDOT:PSS, thermally evaporated HAT-CN, and spin-coated NiO_x NP films. The considerably high component ratio of NiOOH on the air-annealed NiO_x NP film surface results in an enhanced hole injection functionality even without UV–ozone treatment. Consequently, the OLEDs using the NiO_x NP HILs show significantly higher performances than those of the OLEDs using PEDOT:PSS along with a more than doubled lifetime. Moreover, the OLEDs using the NiO_x NP layers show higher external quantum efficiency (EQE), and current and power efficiency values than those of the OLEDs using HAT-CN at a high luminance level. Most notably, the device shows considerably higher current and power efficiency values than those of the recently reported state-of-the-art OLEDs using other types of metal–oxide or metal-based HILs.

1. Introduction

Organic light-emitting diodes (OLEDs) have attracted significant attention in industry and research because of the increasing demand for flat panel displays for televisions, smartphones, tablets, *etc.*, and solid-state lighting applications including flexible and transparent displays.[1–4] Most high-efficiency OLEDs, however, are based on vacuum processes, which have several issues such as high equipment cost, difficulty in processing large areas, and inefficient material use. To address these issues, all or partly solution-processed OLEDs have been studied extensively over the past few years to develop OLEDs *via* a simple and cost-effective manufacturing process on a large area.[5–16] Although significant progress has been accomplished, the device performances of the solution-processed OLEDs are still inferior to those of the vacuum-processed OLEDs. Here, we focus on developing a new solution-processed hole injection layer (HIL) material. To achieve high OLED efficiencies, addition of a HIL between an anode and a hole transport layer (HTL) is necessary because the energy barrier for hole injection from the indium-doped tin oxide (ITO) anode to the HTL limits hole injection into the device, which leads to performance degradation.[17] Poly(3,4-ethylenedioxythiophene):poly(styrenesulfonate) (PEDOT:PSS) is one of the most commonly used hole injection materials for solution-processed OLEDs because of its good hole injection efficiency and high conductivity.[18] Additionally, it can reduce the surface roughness of the ITO and the energy barrier from the ITO to the HTL.[19–25] However, its acidity, inability to block electrons, and tendency to absorb moisture are critical issues that lead to the degradation of device performance and stability.[26–28] On the other hand, 1,4,5,8,9,11-hexaazatriphenylene-hexacarbonitrile (HAT-CN) is commonly employed as a HIL to realize high-efficiency OLEDs. However, vacuum deposition[29–31] is preferred for better performance even though solution-processed HAT-CN[13] has been reported.

Recently, nickel oxide (NiO) has attracted a lot of interest as a semiconducting electrode for supercapacitors,[32] batteries,[33] resistive switching memories,[34] thermistors,[35] and sensors.[36,37] Furthermore, non-stoichiometric NiO (NiO_x) with a large density of Ni^{2+} vacancies is known as one of the rare p-type metal oxides with good hole selectivity and a deep

[a]*Advanced Display Research Center (ADRC), Department of Information Display, Kyung Hee University, 26, Kyungheedae-ro, Dongdaemun-gu, Seoul 02447, Korea. E-mail: jjang@khu.ac.kr*
[b]*Department of Electrical and Computer Engineering, Ajou University, Suwon 16499, Korea*
[c]*Division of Energy Systems Research, Ajou University, Suwon 16499, Korea*
[d]*Department of Mechanical Engineering, University of California, Berkeley, California 94720-1740, USA*
[e]*Department of Mechanical Engineering, Gachon University, Seongnam 13120, Korea. E-mail: dhl@gachon.ac.kr*

† Electronic supplementary information (ESI) available: Fig. S1–S15, Table S1–S4. See DOI: 10.1039/c6nr04643f

valence band that aligns well with the highest occupied molecular orbital (HOMO) levels of many p-type organic semiconductors, whereas near-stoichiometric NiO is a wide band gap insulator with a room temperature conductivity of $\sim 10^{-12}$ S cm^{-1}.[38] Therefore, NiO_x as a HIL and/or HTL in optoelectronic devices is attracting increasing interest. So far, most NiO_x layers have been deposited using vacuum-based processes such as thermal evaporation,[39] sputtering,[40] and pulsed-laser deposition,[41] which require expensive and complicated equipment. Recently, several research studies on solution-processed NiO_x have been reported for solar cell applications.[42–47] For OLED application, sol–gel-derived NiO_x as a HIL has been reported, however, the sol–gel precursor requires a long and high-temperature annealing process (500 °C for 1 h) along with subsequent UV-ozone treatment for enhanced performance.[48]

In this study, we report the development of NP-ink-based NiO_x HILs for high-efficiency OLEDs that can be deposited simply by spin coating. Because the NiO_x NP ink contains ultra-small precrystallized NiO_x NPs, the annealing temperature and time can be decreased significantly, and the resultant thin films have a uniform surface. The results show that the NiO_x NP films can function as effective HILs even without UV-ozone treatment. The OLEDs employing our NiO_x NP HIL show a maximum current efficiency of 73.44 ± 0.39 cd A^{-1} and a power efficiency of 88.32 ± 0.30 lm W^{-1}, which are significantly higher than those of the control OLEDs using PEDOT:PSS, and even higher than those of the control devices using thermally evaporated HAT-CN.

2. Experimental

2.1 NiO_x NP synthesis

NiO_x NPs were synthesized modifying the procedure introduced in the previous studies.[49–51] Under ambient conditions, 257 mg of nickel(II) acetylacetonate ($C_{10}H_{14}NiO_4$) was added to 15 mL of oleylamine ($C_{18}H_{37}N$) and kept at 110 °C for about 1 h to remove the dissolved oxygen and moisture. After cooling the mixture to 90 °C, 0.339 mL of the borane–triethylamine complex ($(C_2H_5)_3N{\cdot}BH_3$) mixed with 2 mL of oleylamine, acting as a reducing agent, was rapidly added to the solution. Then, the resultant solution was maintained at 90 °C for 1 h with vigorous stirring. After cooling down the solution to room temperature, 30 mL of ethanol (C_2H_6O) was added to the solution followed by centrifugation at 3000–4000 rpm to collect the NPs and wash out the organic residuals. The washing step was repeated several times. After discarding the supernatant, the precipitated NPs were dispersed in tetradecane ($C_{14}H_{30}$). The NiO_x NP dispersion was stable for more than 3 weeks in a sealed vial stored in the shelf even though we did not test the stability for longer periods.

2.2 OLED fabrication

OLEDs were fabricated on ITO-precoated glass substrates. The sheet resistance of the substrate with a 170 nm thick ITO layer was 9 Ω sq^{-1}. The ITO substrate was cleaned by ultrasonication in acetone, methanol, and isopropanol sequentially for 15 min each. Then, it was treated with UV-ozone for 15 min to increase its work function and to improve adhesion to HILs. We used three different HILs on the ITO substrates: thermally evaporated HAT-CN, solution-processed PEDOT:PSS, and NiO_x NP thin films. PEDOT:PSS was spin-coated on the ITO substrate and was cured at 160 °C in a glove box filled with N_2 to remove the solvent. NiO_x NP ink was spin-coated on the ITO, and then annealed at 100–300 °C for various times in air or under an N_2 environment. HAT-CN layers were deposited by thermal evaporation. The reference thickness of the HILs was fixed at 20 nm. Then, NPB as a HTL, TCTA as an exciton blocking layer (EBL), TCTA:TPBi:Ir(ppy)$_3$ (3 : 7 molar ratio and 12 wt%) as an EML, TPBi as an electron transport layer (ETL), and LiF and Al as cathodes were deposited consecutively by thermal evaporation in a vacuum chamber. To investigate the thickness effect of the NiO_x HIL, various thicknesses of NiO_x layers were prepared by controlling the ink concentration and spin speed.

2.3 Device characterization

XRD data of the prepared films were obtained using a Rigaku Ultima III high-resolution X-ray diffractometer. AFM and TEM images were obtained using a PSIA XE 100 and a JEOL JEM-2100F, respectively. The transmittance and absorbance data of the NiO_x NP film were obtained at room temperature with a SCINCO S4100 spectrophotometer. A Konica Minolta CS100A luminance meter and a Keithley 2635A source meter were used to measure the *J–V–L*, and current and power efficiencies, respectively. A CS1000A spectrometer coupled with a Keithley 2635A source meter was used to measure the EL spectrum and the EQE. The lifetime was measured using a PolaronixTM M6000 OLED lifetime system in air.

3. Results and discussion

The as-synthesized NiO_x NPs observed using transmission electron microscopy (TEM) are 3–5 nm in diameter, as shown in Fig. 1a. The high-resolution TEM (HRTEM) and selected area electron diffraction (SAED) pattern displayed in the inset of Fig. 1a and b, respectively, confirm that the NPs have a well-defined cubic crystalline structure even without any post-treatment. The NiO_x NP thin film was prepared by spin coating the NiO_x NP ink. The atomic force microscopy (AFM) image of the surface of the film prepared by spin coating the NiO_x NP ink on an ITO-precoated glass substrate is presented in Fig. 1c. It confirms the formation of an ultra-smooth surface of the NiO_x NP thin film with a root mean square (RMS) roughness value of 1.18 nm, which is attributed to the well-dispersed ink containing evenly sized, very small NPs. The crystal structure of the NiO_x NP thin film, annealed in air at 270 °C for 10 min to remove organic residuals was analyzed by X-ray diffraction (XRD). The recorded XRD pattern displayed in Fig. 1d shows sharp peaks at 2θ = 37.2°, 43.3°, 62.9°, 75.4°, and 79.4°, which correspond to the (111), (200), (220), (311), and (222) crystal

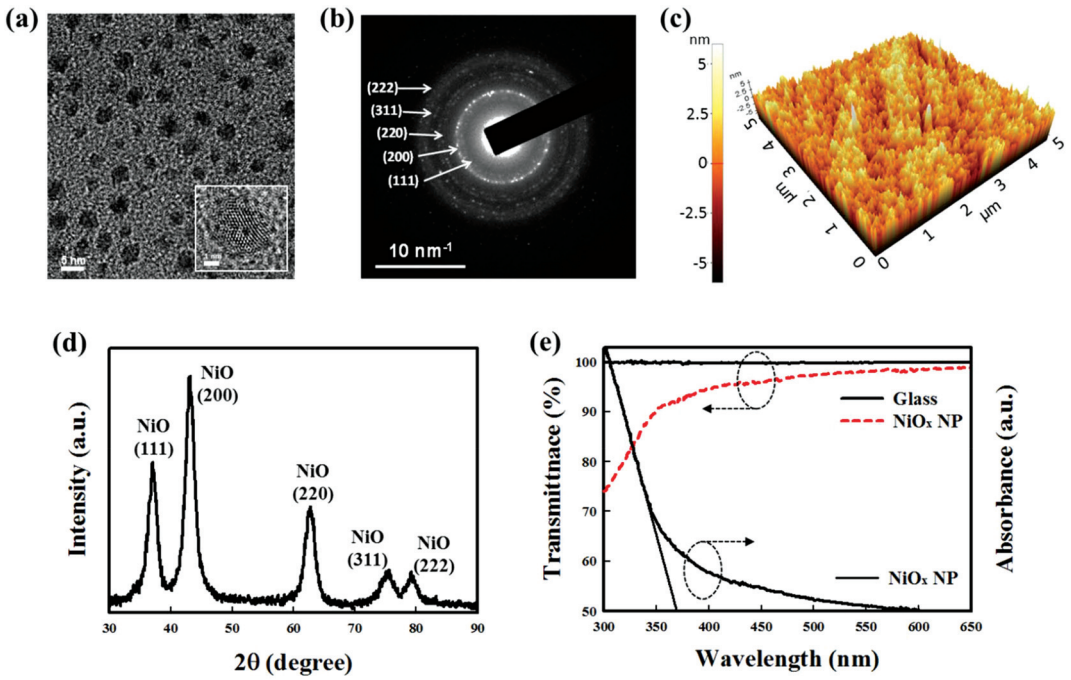

Fig. 1 (a) TEM image of NiO_x NPs. The inset shows the HRTEM of the 3–5 nm NiO_x NPs. (b) SAED pattern of the NiO_x NP. (c) AFM image of the NiO_x NP film. (d) XRD pattern of the NiO_x NP film. The peaks at 2θ = 37.1°, 43.4°, 63.1° 75.4°, and 79.4° are attributed to the (111), (200), (220), (311), and (222) crystal planes, respectively, of the NiO_x NP with a FCC structure. (e) Optical transmittance (referenced to bare glass) and absorbance spectra of the 20 nm thick NiO_x NP film deposited on glass. The optical band gap of the NiO_x NP, 3.36 eV, was calculated from the absorbance spectra.

planes of the NiO_x NP with a face-centered cubic (FCC) system, respectively.[52] It is worth noting that since the film is composed of precrystallized NPs, the annealing temperature and time required for a crystallized NiO_x NP thin film can be significantly decreased compared to those for the sol–gel-derived NiO_x film.[45] It is also noted that increasing annealing time at 270 °C shows no additional effect on the properties of the layer. The transmittance and absorbance spectra of the 20 nm thick NiO_x NP film which was spin-coated and annealed on bare glass are shown in Fig. 1e. The transmittance is over 94% in the visible region when bare glass is used as a reference. As the thickness of the NiO_x NP layer increases from 20 to 145 nm, the transmittance at 550 nm wavelength decreases from 98.0% to 86.4% (Fig. S1†). The optical band gap of the NiO_x NP thin film, which can be obtained from the absorbance spectrum and calculated using Tauc's equation,[53] is 3.36 eV.

To investigate the chemical and electronic states of the elements in the NiO_x NP film, we analyzed the surface composition of the film by X-ray photoelectron spectroscopy (XPS). Because the properties of the metal oxide are influenced by the annealing environment, an analysis of the NiO_x film annealed in N_2 was also conducted for comparison. Fig. S2† shows the XPS spectra of Ni $2p_{3/2}$ and O 1s obtained from the NiO_x NP films annealed in N_2 or air at 270 °C for 10 min. As depicted in Fig. S2a and b,† the Ni $2p_{3/2}$ spectrum of the N_2-annealed NiO_x NP film indicates three distinct peaks at 854.28, 856.28, and 861.18 eV that correspond to Ni^{2+} in the standard NiO, Ni^{2+} in the nickel hydroxide ($Ni(OH)_2$), and a shake-up peak, respectively, while the O 1s spectrum of the N_2-annealed film shows two distinct peaks at 529.68 and 531.38 eV that are ascribed to NiO and $Ni(OH)_2$, respectively.[54–56] The $Ni(OH)_2$ peaks are attributed to defective NiO with hydroxyl groups adsorbed on the surface.[57,58] Fig. S2c and d† show the XPS spectra of the air-annealed NiO_x NP film. The three peaks located at binding energies of 853.99, 855.48, and 860.98 eV in the Ni $2p_{3/2}$ spectra correspond to Ni^{2+} in standard NiO, Ni^{2+} in $Ni(OH)_2$, and a shake-up peak, respectively,[54–57,59–62] which are also found in the N_2-annealed film. The two peaks at 529.38 and 531.08 eV in the O 1s spectrum confirm the presence of NiO and $Ni(OH)_2$, respectively. Interestingly, new species were found on the air-annealed NiO_x NP film, which can be confirmed by the additional peaks at 856.68 eV in the Ni $2p_{3/2}$ spectrum and at 531.98 eV in the O 1s spectrum. The peaks indicate the presence of Ni^{3+} in oxy-hydroxides (NiOOH).[59] The component ratios calculated from the XPS peak intensities of NiOOH on the air-annealed NiO_x NP film are 23.05% and 21.18% for Ni $2p_{3/2}$ and O 1s, respectively. The binding energies and the component ratios of the Ni $2p_{3/2}$ and O 1s signals on the air-annealed NiO_x NP film are summarized in Table S1.† It should be noted that our air-annealed, UV-ozone untreated NiO_x NP film has a much higher component ratio of NiOOH than those reported in the literature for the sol–gel-derived NiO_x film (15.3% for Ni $2p_{3/2}$, and 14.7% for O 1s).[48] Considering that the origin of the conductivity of NiO_x comes from Ni^{2+} vacancies accompanied by compensation of the holes or Ni^{3+},[48,64] the air-annealed NiO_x is expected to have

higher conductivity. Moreover, we can appropriately infer that a higher dipolar NiOOH component ratio induces enhanced hole injection from the NiO_x NP layer to the HTL because the dipolar NiOOH surface species on the film result in an increase in the band gap energy level *via* a vacuum-level shift.[64] These hypotheses are verified by experimental data which will be presented later.

To evaluate the hole injection functionality of the NiO_x NP layer, we fabricated OLEDs having a structure of ITO/NiO_x/*N*,*N*′-di(naphthalene-1-yl)-*N*,*N*′-diphenylbenzidine (NPB)/4,4′,4″-tris(carbazol-9-yl)-triphenylamine (TCTA)/TCTA:2,2′,2″-(1,3,5-benzenetriyl)-tris-[1-phenyl-1-*H*-benzimidazole] (TPBi):12% tris(2-phenylpyridinato-C2,N)iridium(III) (Ir(ppy)$_3$)/TPBi/LiF/Al, and characterized their performance. UV photoelectron spectroscopy (UPS) was utilized to investigate the energy band structures of the air-annealed NiO_x NP film. In addition, the band structures of HAT-CN and PEDOT:PSS, which were used as the HILs of OLEDs for performance comparison in this study, were also investigated. The work functions can be obtained by the intercept between the background level and the extrapolation of the leading edge in the secondary electron cut-off region in the UPS spectra. As shown in Fig. 2a, the work functions of the ITO, HAT-CN, PEDOT:PSS and NiO_x NP were determined to be 4.21, 5.34, 4.55, and 4.86 eV, respectively. Fig. 2b–e show that the HOMO level of the HAT-CN on the ITO is found to be about 3.72 eV lower than the Fermi level of the ITO, while the valence band edges of the PEDOT:PSS and NiO_x NP films are 0.59 and 0.53 eV below the ITO Fermi level, respectively. The ionization potentials (E_{ion}) are calculated by the sum of the work functions and the valence band edge energy.[63] Therefore, the values of E_{ion} for the HAT-CN, PEDOT:PSS, and NiO_x NP films are determined as follows:

$$E_{ion}\ (\text{HAT-CN}) = 5.34\ \text{eV} + 3.72\ \text{eV} = 9.06\ \text{eV}.$$

$$E_{ion}\ (\text{PEDOT : PSS}) = 4.55\ \text{eV} + 0.59\ \text{eV} = 5.14\ \text{eV}.$$

$$E_{ion}\ (NiO_x\ \text{NP}) = 4.86\ \text{eV} + 0.53\ \text{eV} = 5.39\ \text{eV}.$$

The E_{ion} of the NiO_x NP is deeper than that of PEDOT:PSS, and is adjacent to the HOMO levels of hole transport materials (5.3–5.5 eV). Therefore, the NiO_x NP is a suitable HIL for OLEDs. The optical band gaps of HAT-CN were obtained from the absorption onsets, which are calculated to be 3.80 (Fig. S3†). As a result, the energy level band diagram and the cross sectional schematic of OLEDs using NiO_x can be illus-

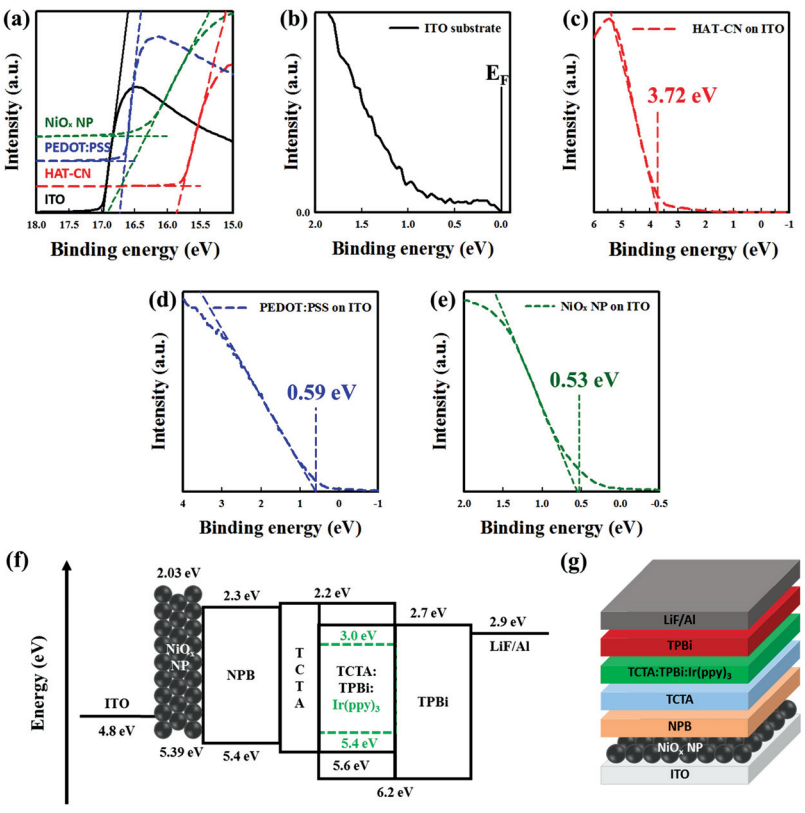

Fig. 2 He(I) UPS spectra of HAT-CN, PEDOT:PSS, and the NiO_x NP deposited on the ITO substrate; (a) secondary electron cutoff regions. (b), (c), (d), and (e) Valence band edge regions of the ITO substrate, HAT-CN, PEDOT:PSS, and NiO_x NP on ITO, respectively. The work functions are calculated from the secondary electron cutoff positions of ITO (16.99 eV), HAT-CN (15.86 eV), PEDOT:PSS (16.65 eV), and NiO_x NP (16.34 eV), which are 4.21, 5.34, 4.55, and 4.86 eV, respectively. (f) Energy level band diagram of the green phosphorescent OLEDs using the air-annealed NiO_x NP HIL. (g) Cross sectional schematic of the OLEDs.

trated as shown in Fig. 2f and g. The energy level band diagrams of OLEDs using other HILs are depicted in Fig. S4.†

Fig. 3 shows the current density–voltage (*J–V*) characteristics of the OLEDs using 20 nm thick NiO_x NP HILs annealed for 10 min under different conditions. As shown in Fig. 3a, the OLED using the air-annealed NiO_x NP HIL exhibits superior *J–V* characteristics with a low turn-on voltage, whereas the OLED using the N_2-annealed HIL exhibits negligible current flow. As mentioned above, the conductivity of the NiO_x film depends strongly on the defect structure of NiO_x and it increases as more Ni^{3+} (NiOOH) ions occupy the vacant positions of Ni^{2+}. Because NiOOH was not detected in the N_2-annealed NiO_x NP film, the NiO_x NP film becomes less conductive, hence, resulting in negligible current flow. To further support this argument, we fabricated hole only devices (HODs) using each NiO_x layer to investigate the electrical conductivity characteristics. As shown in Fig. S5,† the current density of the HOD using air-annealed NiO_x is higher by two orders of magnitude at 2.5 V which is near the turn-on voltage of the OLEDs, and over 1000 times higher at 6 V than that using the N_2-annealed one. This experimental data supports that the air-annealed NiO_x NP layer has a higher hole conductivity. We also investigated the energy level difference of each NiO_x as shown in Fig. S6 and S7.† Air-annealed NiO_x has a substantially low injection barrier to the HOMO of NPB, and thus has enhanced hole transport characteristics. Fig. 3b shows the *J–V* characteristics of OLEDs using the NiO_x NP HILs annealed in air for 10 min at different temperatures. The current density increases as the annealing temperature increases from 100 °C to 270 °C, whereas an increase in the annealing temperature from 270 °C to 300 °C shows almost no difference in the *J–V* characteristics. The low current density is possibly due to the residual organic compounds in the HIL, which is verified as shown in Fig. S8–S10.† Further details are discussed in the ESI.† To investigate the thickness effect, the NiO_x film thickness was adjusted to 20–145 nm by controlling the ink concentration and spin coating speed. The current density–voltage–luminance (*J–V–L*) characteristics of the OLEDs using the NiO_x NP HIL with different thicknesses are shown in Fig. S11a and S12a.† The devices with thinner HILs have a higher current density, which indicates that thinner HILs have higher conductance due to the shorter distance that the holes have to travel. The OLEDs with thinner NiO_x show a higher luminance as well at a certain voltage, which is ascribed to the balanced charge carriers in the EML and higher transmittance of the NiO_x NP layer. The OLEDs with thinner NiO_x also have higher current efficiency and power efficiency as presented in Fig. S11b and S12b.† However, the difference of the efficiency values is not evident for NiO_x layers over the range of 20–45 nm, which reveals that no remarkable current leakage occurs. Whereas, as the NiO_x layer becomes thinker than 45 nm, noticeable efficiency degradation is observed, which may be attributed to the high resistance of the NiO_x layer and high current leakage through the layer owing to the long carrier path. Further performance characterization was performed for the OLEDs with 20–45 nm thick NiO_x layers as shown in Fig. S13 and Table S2.† Normalized electroluminescence (EL) spectra of OLEDs at the same brightness of 10 000 cd m^{-2} show almost the same EL spectrum regardless of the HIL thickness (Fig. S13a†). To investigate the stability, we measured the luminance over time while the OLEDs were driven at constant current with an initial luminance value L_0 = 1000 cd m^{-2}. The OLED using the 20 nm NiO_x NP HIL shows a longer lifetime than the OLEDs using thicker HILs (Fig. S13b†), which may be due to the lower driving voltage and current density at the same luminance compared to the OLEDs using thicker HILs (Table S2, Fig. S13c†).

The performance of OLEDs with the three types of HILs (thermally evaporated HAT-CN, solution-processed PEDOT:PSS, and NiO_x NP) was compared. The OLEDs with all the HILs have the same structure, ITO/HIL/NPB/TCTA/TCTA:TPBi:12% $Ir(ppy)_3$/TPBi/LiF/Al. To determine the reproducibil-

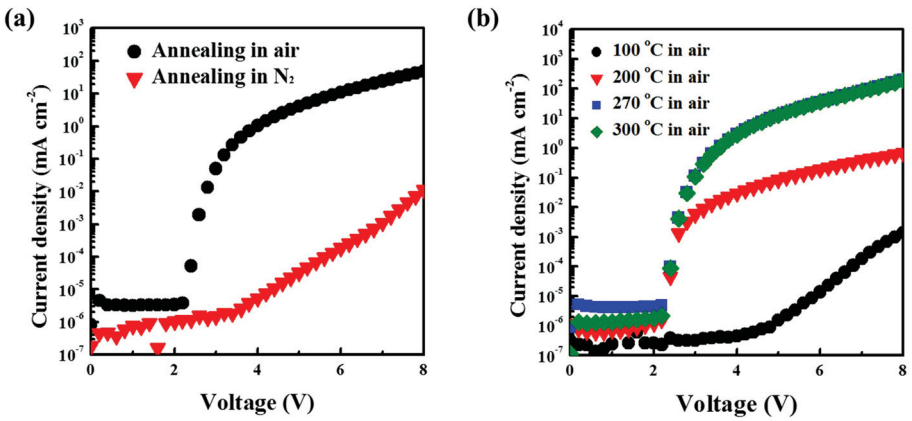

Fig. 3 (a) *J–V* characteristics of the OLEDs using the NiO_x NP annealed at 270 °C for 10 min in different environments. The OLED using the NiO_x NP upon annealing in N_2 exhibits negligible current flow. (b) *J–V* characteristics of the OLEDs using the NiO_x NP annealed in air for 10 min at different temperatures. The current density increases as the annealing temperature increases from 100 °C to 270 °C. Meanwhile, the OLEDs using the NiO_x NP HIL annealed at 270 °C or 300 °C show almost identical *J–V* curves.

ity of the device performance, a total of 63 devices (21 devices for each HIL) were fabricated. The performance plots of the representative OLED samples with each HIL are presented in Fig. 4. Fig. 4a shows the *J–V–L* characteristics of OLEDs with each HIL, and the representative values are summarized in Table S3.† The OLED with the NiO_x NP HIL has a lower turn-on voltage of 2.46 V and a lower driving voltage of 3.67 V than OLEDs with the HAT-CN and PEDOT:PSS HILs. Moreover, the OLED with the NiO_x NP HIL exhibits a higher luminance, more than 1.4 times at 8 V, than OLEDs with other HILs. Fig. 4(b) shows the current efficiency–luminance and power efficiency–luminance characteristics, which confirm the superior efficiencies of the OLED with the NiO_x NP HIL. The histograms of the maximum current and power efficiencies of 21 OLED devices with each HIL are shown in Fig. S14.† The solid lines in the plots indicate Gaussian fittings. The average values of the maximum current and power efficiencies, the current and power efficiencies at 1000 cd m^{-2} and 10 000 cd m^{-2} of the 21 OLEDs using each HIL are summarized in Table 1. The average values of the maximum current and power efficiency of the OLEDs with the NiO_x NP HILs are significantly higher than those of the OLEDs with the PEDOT:PSS HIL, and are even higher than those of OLEDs using the thermally evaporated HAT-CN HIL. In particular, the OLEDs with the NiO_x NP HIL have 34% higher power efficiencies than those of the OLEDs with PEDOT:PSS at 1000 cd m^{-2}, and have 10% higher power efficiencies that those of the OLEDs with HAT-CN at 10 000 cd m^{-2}. The average values are also presented as graphs in Fig. S15† for easy visual comparison. Fig. 4c shows the external quantum efficiency (EQE) characteristics of representative OLED samples with each HIL. The OLED with the NiO_x NP HIL has the highest EQE of 25.54%,

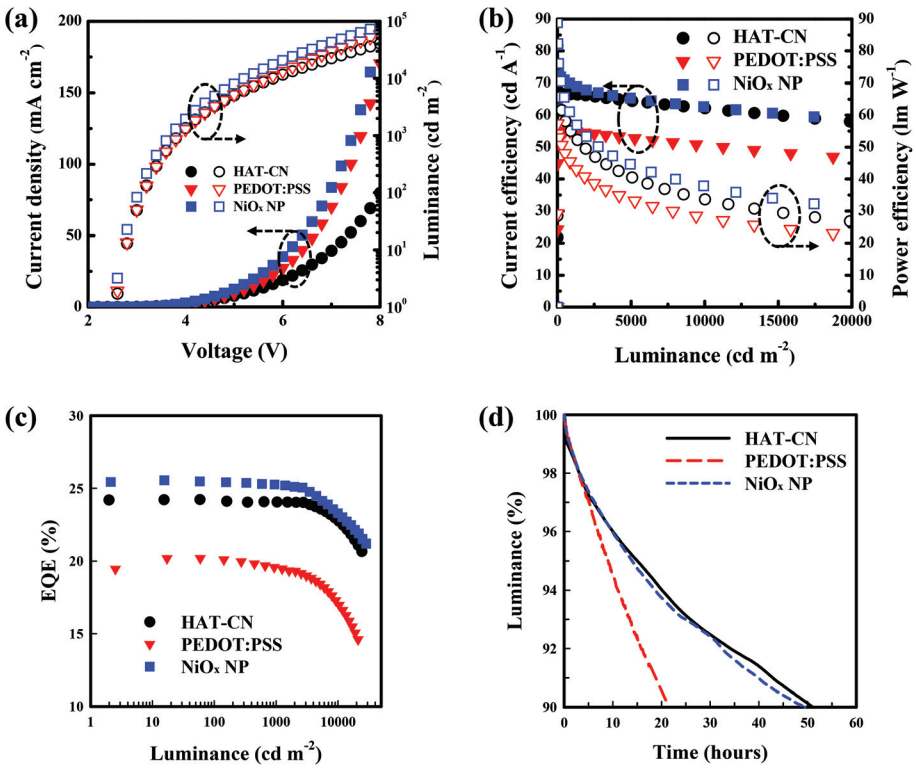

Fig. 4 Performance of OLEDs with various HILs; (a) *J–V–L* characteristics, (b) current efficiency–luminance and power efficiency–luminance characteristics, (c) EQE as a function of luminance, and (d) lifetime (L_{90}) with an initial luminance L_0 = 1000 cd m^{-2} of the OLEDs with various HILs.

Table 1 The average current and power efficiencies of the OLEDs at the maximum, at 1000 cd m^{-2}, and at 10 000 cd m^{-2}, collected from 21 devices

	Maximum		At 1000 cd m^{-2}		At 10 000 cd m^{-2}	
HILs	Current efficiency (cd A^{-1})	Power efficiency (lm W^{-1})	Current efficiency (cd A^{-1})	Power efficiency (lm W^{-1})	Current efficiency (cd A^{-1})	Power efficiency (lm W^{-1})
HAT-CN	68.69 ± 0.27	82.52 ± 0.34	67.96 ± 0.65	54.31 ± 0.13	63.22 ± 0.62	31.72 ± 0.96
PEDOT:PSS	55.42 ± 0.13	57.41 ± 0.14	54.27 ± 0.42	44.03 ± 0.36	50.26 ± 0.22	28.44 ± 0.45
NiO_x NP	73.44 ± 0.39	88.32 ± 0.30	69.23 ± 0.37	59.00 ± 0.25	62.40 ± 0.72	34.87 ± 0.15

which is higher than that of OLEDs with PEDOT:PSS (20.19%) and HAT-CN (24.22%) HILs. The stability of the OLEDs was evaluated by measuring the luminance over time while the OLEDs were driven at constant current in air. The L_{90} lifetime characteristics of OLEDs with an initial luminance of 1000 cd m^{-2} are shown in Fig. 4d, where L_{90} is defined as the time taken for the luminance to drop to 90% of the initial value under continuous operation. The lifetime of the OLED employing the NiO_x NP HIL is more than twice that of the OLED using PEDOT:PSS. More importantly, the OLED with the NiO_x NP HIL shows a similar lifetime curve compared with the OLED with HAT-CN. Table S4† shows a summary of the performance of a green phosphorescent OLED with different types of metal–oxide[48,65–67] or metal-based[68] HILs in the recently published literature. Notably, our device using the NiO_x NP HIL and exhibiting current and power efficiency values of 69.23 cd A^{-1} and 59.00 lm W^{-1} at 1000 cd m^{-2}, respectively, outperforms other devices in the list.

4. Conclusions

In conclusion, NiO_x NPs with a particle size of 3–5 nm were synthesized and NP films were introduced as a new HIL, replacing conventional materials, to fabricate OLEDs. The considerably high component ratio of NiOOH on the air-annealed NiO_x NP film surface results in an enhanced hole injection functionality even without UV-ozone treatment. OLEDs with the NiO_x NP HIL show a maximum current and power efficiency of 73.44 ± 0.39 cd A^{-1} and 88.32 ± 0.30 lm W^{-1}, respectively, which are significantly higher than those of the OLEDs with PEDOT:PSS, and are even higher than those of the OLEDs with thermally evaporated HAT-CN. Moreover, OLEDs with the NiO_x NP HIL have a power efficiency of 34.87 ± 0.15 lm W^{-1} at 10 000 cd m^{-2}, which is 10% and 22% higher than those of the OLEDs with HAT-CN and PEDOT:PSS HILs, respectively. The devices with the NiO_x NP HIL also have lower turn-on and driving voltages, and have a higher maximum EQE (25.54%) than those with HAT-CN (24.22%) and PEDOT:PSS (20.19%) HILs. Most notably, the device shows current and power efficiency values of 69.23 cd A^{-1} and 59.00 lm W^{-1} at 1000 cd m^{-2}, respectively, which are considerably higher than those of the state-of-the-art green OLEDs using other types of metal–oxide or metal-based HILs. The L_{90} lifetime of the OLEDs employing the NiO_x NP HIL is more than 2 times that of the OLEDs using PEDOT:PSS, and is similar to those using thermally evaporated HAT-CN. We believe the results of this study will be of great interest to those involved in research on OLEDs as well as a variety of optoelectronic devices.

Acknowledgements

This work was supported by the Human Resources Development program (Grant No. 20134010200490) of the Korea Institute of Energy Technology Evaluation and Planning (KETEP) grant funded by the Korea government Ministry of Trade, Industry and Energy, and by the Basic Science Research Program through the National Research Foundation of Korea (NRF) funded by the Ministry of Science, ICT & Future Planning (NRF-2015R1C1A1A02037541).

References

1 C. Murawski, K. Leo and M. C. Gather, *Adv. Mater.*, 2013, **25**, 6801–6827.
2 G. M. Farinola and R. Ragni, *Chem. Soc. Rev.*, 2011, **40**, 3467–3482.
3 Q. Wang and D. Ma, *Chem. Soc. Rev.*, 2010, **39**, 2387–2398.
4 L. Xiao, Z. Chen, B. Qu, J. Luo, S. Kong, Q. Gong and J. Kido, *Adv. Mater.*, 2011, **23**, 926–952.
5 R. Friend, R. Gymer, A. Holmes, J. Burroughes, R. Marks, C. Taliani, D. Bradley, D. Dos Santos, J. Bredas and M. Lögdlund, *Nature*, 1999, **397**, 121–128.
6 P. K. Ho, J. S. Kim, J. H. Burroughes, H. Becker, S. F. Li, T. M. Brown, F. Cacialli and R. H. Friend, *Nature*, 2000, **404**, 481–484.
7 H. Youn, K. Jeon, S. Shin and M. Yang, *Org. Electron.*, 2012, **13**, 1470–1478.
8 H.-Y. Oh, C. Kulshreshtha, J. H. Kwon and S. Lee, *Org. Electron.*, 2010, **11**, 1624–1630.
9 C. A. Zuniga, J. Abdallah, W. Haske, Y. Zhang, I. Coropceanu, S. Barlow, B. Kippelen and S. R. Marder, *Adv. Mater.*, 2013, **25**, 1739–1744.
10 B. Zhang, G. Tan, C. S. Lam, B. Yao, C. L. Ho, L. Liu, Z. Xie, W. Y. Wong, J. Ding and L. Wang, *Adv. Mater.*, 2012, **24**, 1873–1877.
11 Y. J. Doh, J. S. Park, W. S. Jeon, R. Pode and J. H. Kwon, *Org. Electron.*, 2012, **13**, 586–592.
12 B. S. Du, J. L. Liao, M. H. Huang, C. H. Lin, H. W. Lin, Y. Chi, H. A. Pan, G. L. Fan, K. T. Wong and G. H. Lee, *Adv. Funct. Mater.*, 2012, **22**, 3491–3499.
13 H.-W. Lin, W.-C. Lin, J.-H. Chang and C.-I. Wu, *Org. Electron.*, 2013, **14**, 1204–1210.
14 W.-C. Lin, W.-C. Huang, M.-H. Huang, C.-C. Fan, H.-W. Lin, L.-Y. Chen, Y.-W. Liu, J.-S. Lin, T.-C. Chao and M.-R. Tseng, *J. Mater. Chem. C*, 2013, **1**, 6835–6841.
15 J. Wu, M. Agrawal, H. A. Becerril, Z. Bao, Z. Liu, Y. Chen and P. Peumans, *ACS Nano*, 2009, **4**, 43–48.
16 M. Zhang, S. Höfle, J. Czolk, A. Mertens and A. Colsmann, *Nanoscale*, 2015, **7**, 20009–20014.
17 J. H. Youn, Y. I. Lee, M. S. Ryu, A. Elschner, W. Lövenich, A. Scheel, H. T. Moon and J. Jang, *J. Electrochem. Soc.*, 2011, **158**, J321–J325.
18 M. De Jong, L. Van Ijzendoorn and M. De Voigt, *Appl. Phys. Lett.*, 2000, **77**, 2255–2257.
19 W. Kim, A. Mäkinen, N. Nikolov, R. Shashidhar, H. Kim and Z. Kafafi, *Appl. Phys. Lett.*, 2002, **80**, 3844–3846.
20 D. Heithecker, A. Kammoun, T. Dobbertin, T. Riedl, E. Becker, D. Metzdorf, D. Schneider, H.-H. Johannes and W. Kowalsky, *Appl. Phys. Lett.*, 2003, **82**, 4178–4180.

21 C. Jonda, A. Mayer, U. Stolz, A. Elschner and A. Karbach, *J. Mater. Sci.*, 2000, **35**, 5645–5651.
22 T. Brown, J. Kim, R. Friend, F. Cacialli, R. Daik and W. Feast, *Appl. Phys. Lett.*, 1999, **75**, 1679–1681.
23 S. Kirchmeyer and K. Reuter, *J. Mater. Chem.*, 2005, **15**, 2077–2088.
24 S. Karg, J. Scott, J. Salem and M. Angdopoulos, *Synth. Met.*, 1996, **80**, 111–117.
25 A. Kanwat and J. Jang, *J. Mater. Chem. C*, 2014, **2**, 901–907.
26 M. Jørgensen, K. Norrman and F. C. Krebs, *Sol. Energy Mater. Sol. Cells*, 2008, **92**, 686–714.
27 H. Yan, B. J. Scott, Q. Huang and T. J. Marks, *Adv. Mater.*, 2004, **16**, 1948–1953.
28 J. R. Manders, S. W. Tsang, M. J. Hartel, T. H. Lai, S. Chen, C. M. Amb, J. R. Reynolds and F. So, *Adv. Funct. Mater.*, 2013, **23**, 2993–3001.
29 D. H. Kim and T. W. Kim, *Org. Electron.*, 2014, **15**, 3452–3457.
30 H. Sun, Q. Guo, D. Yang, Y. Chen, J. Chen and D. Ma, *ACS Photonics*, 2015, **2**, 271–279.
31 Y. Dai, H. Zhang, Z. Zhang, Y. Liu, J. Chen and D. Ma, *J. Mater. Chem. C*, 2015, **3**, 6809–6814.
32 F.-B. Zhang, Y.-K. Zhou and H.-L. Li, *Mater. Chem. Phys.*, 2004, **83**, 260–264.
33 B. Li, H. Cao, J. Shao, H. Zheng, Y. Lu, J. Yin and M. Qu, *Chem. Commun.*, 2011, **47**, 3159–3161.
34 U. Russo, D. Ielmini, C. Cagli and A. L. Lacaita, *IEEE Trans. Electron Devices*, 2009, **56**, 186–192.
35 C. C. Huang, Z. K. Kao and Y. C. Liao, *ACS Appl. Mater. Interfaces*, 2013, **5**, 12954–12959.
36 C. Alcock, B. Li, J. Fergus and L. Wang, *Solid State Ionics*, 1992, **53**, 39–43.
37 H. Kumagai, M. Matsumoto, K. Toyoda and M. Obara, *J. Mater. Sci. Lett.*, 1996, **15**, 1081–1083.
38 M. A. Wittenauer and L. Van Zandt, *Philos. Mag. B*, 1982, **46**, 659–667.
39 W. Yu, L. Shen, S. Ruan, F. Meng, J. Wang, E. Zhang and W. Chen, *Sol. Energy Mater. Sol. Cells*, 2012, **98**, 212–215.
40 X. Fan, G. Fang, F. Cheng, P. Qin, H. Huang and Y. Li, *J. Phys. D: Appl. Phys.*, 2013, **46**, 305106.
41 M. D. Irwin, D. B. Buchholz, A. W. Hains, R. P. Chang and T. J. Marks, *Proc. Natl. Acad. Sci. U. S. A.*, 2008, **105**, 2783–2787.
42 B. Mustafa, J. Griffin, A. S. Alsulami, D. G. Lidzey and A. R. Buckley, *Appl. Phys. Lett.*, 2014, **104**, 063302.
43 F. Jiang, W. C. Choy, X. Li, D. Zhang and J. Cheng, *Adv. Mater.*, 2015, **27**, 2930–2937.
44 X. Yin, P. Chen, M. Que, Y. Xing, W. Que, C. Niu and J. Shao, *ACS Nano*, 2016, **10**, 3630–3636.
45 J. H. Kim, P. W. Liang, S. T. Williams, N. Cho, C. C. Chueh, M. S. Glaz, D. S. Ginger and A. K. Y. Jen, *Adv. Mater.*, 2015, **27**, 695–701.
46 Z. Zhai, X. Huang, M. Xu, J. Yuan, J. Peng and W. Ma, *Adv. Energy Mater.*, 2013, **3**, 1614–1622.
47 U. Kwon, B.-G. Kim, D. C. Nguyen, J.-H. Park, N. Y. Ha, S.-J. Kim, S. H. Ko, S. Lee, D. Lee and H. J. Park, *Sci. Rep.*, 2016, **6**, 30759.
48 S. Liu, R. Liu, Y. Chen, S. Ho, J. H. Kim and F. So, *Chem. Mater.*, 2014, **26**, 4528–4534.
49 Ö. Metin, S. Özkar and S. Sun, *Nano Res.*, 2010, **3**, 676–684.
50 D. Lee, D. Paeng, H. K. Park and C. P. Grigoropoulos, *ACS Nano*, 2014, **8**, 9807–9814.
51 Y. Rho, K.-T. Kang and D. Lee, *Nanoscale*, 2016, **8**, 8976–8985.
52 T. J. Macdonald, J. Xu, S. Elmas, Y. J. Mange, W. M. Skinner, H. Xu and T. Nann, *Nanomaterials*, 2014, **4**, 256–266.
53 D. Wood and J. Tauc, *Phys. Rev. B: Solid State*, 1972, **5**, 3144.
54 K. Kim and N. Winograd, *Surf. Sci.*, 1974, **43**, 625–643.
55 S. Uhlenbrock, C. Scharfschwerdt, M. Neumann, G. Illing and H.-J. Freund, *J. Phys.: Condens. Matter*, 1992, **4**, 7973.
56 B. Sasi and K. Gopchandran, *Nanotechnology*, 2007, **18**, 115613.
57 M. Langell and M. Nassir, *J. Phys. Chem.*, 1995, **99**, 4162–4169.
58 S.-Y. Han, D.-H. Lee, Y.-J. Chang, S.-O. Ryu, T.-J. Lee and C.-H. Chang, *J. Electrochem. Soc.*, 2006, **153**, C382–C386.
59 E. L. Ratcliff, J. Meyer, K. X. Steirer, A. Garcia, J. J. Berry, D. S. Ginley, D. C. Olson, A. Kahn and N. R. Armstrong, *Chem. Mater.*, 2011, **23**, 4988–5000.
60 N. Kitakatsu, V. Maurice, C. Hinnen and P. Marcus, *Surf. Sci.*, 1998, **407**, 36–58.
61 B. Payne, M. Biesinger and N. McIntyre, *J. Electron Spectrosc. Relat. Phenom.*, 2009, **175**, 55–65.
62 M. Langell, C. Berrie, M. Nassir and K. Wulser, *Surf. Sci.*, 1994, **320**, 25–38.
63 R. Schlaf, B. Parkinson, P. Lee, K. Nebesny and N. Armstrong, *J. Phys. Chem. B*, 1999, **103**, 2984–2992.
64 S. Nandy, B. Saha, M. K. Mitra and K. Chattopadhyay, *J. Mater. Sci.*, 2007, **42**, 5766–5772.
65 J. Meyer, S. Hamwi, T. Bülow, H.-H. Johannes, T. Riedl and W. Kowalsky, *Appl. Phys. Lett.*, 2007, **91**, 113506.
66 H. Lee, Y. Kwon and C. Lee, *J. Soc. Inf. Disp.*, 2012, **20**, 640–645.
67 Q. Fu, J. Chen, C. Shi and D. Ma, *ACS Appl. Mater. Interfaces*, 2013, **5**, 6024–6029.
68 A. Perumal, H. Faber, N. Yaacobi-Gross, P. Pattanasattayavong, C. Burgess, S. Jha, M. A. McLachlan, P. N. Stavrinou, T. D. Anthopoulos and D. D. Bradley, *Adv. Mater.*, 2015, **27**, 93–100.